Journal of Power Sources 246 (2014) 365–370

Contents lists available at ScienceDirect

Journal of Power Sources

journal homepage: www.elsevier.com/locate/jpowsour

Structure and electrochemical properties of $LiNi_{0.5}Mn_{1.5}O_4$ epitaxial thin film electrodes

Hiroaki Konishi, Kota Suzuki, Sou Taminato, Kyungsu Kim, Sangryun Kim, Jaemin Lim, Masaaki Hirayama, Ryoji Kanno*

Department of Electronic Chemistry, Interdisciplinary Graduate School of Science and Engineering, Tokyo Institute of Technology, 4259 Nagatsuta-cho, Midori-ku, Yokohama 226-8502, Japan

HIGHLIGHTS

- Epitaxial $LiNi_{0.5}Mn_{1.5}O_4$ films are synthesized on the $SrTiO_3$ substrates.
- The manganese valence of $LiNi_{0.5}Mn_{1.5}O_4$ films changes with film thickness.
- Electrochemical properties depend on the film thickness and orientation.

ARTICLE INFO

Article history:
Received 1 June 2013
Received in revised form
8 July 2013
Accepted 9 July 2013
Available online 24 July 2013

Keywords:
$LiNi_{0.5}Mn_{1.5}O_4$
Epitaxial thin film
Surface structure
High voltage positive electrode
Lithium ion battery

ABSTRACT

The structure and electrochemical properties of epitaxial thin film $LiNi_{0.5}Mn_{1.5}O_4$ electrodes are investigated for lithium ion secondary batteries applications. The orientation and thickness of the $LiNi_{0.5}Mn_{1.5}O_4$ films are controlled by changing the substrate orientation and the pulse laser deposition time, respectively. The lattice parameters of the films increase with film thickness and the manganese valence decreases without any change in the nickel valence. Regardless of their orientation, all the films exhibit reversible capacities of 80–130 mAh g^{-1}. The dependence of the discharge capacity on film thickness indicates a nanosize effect. The electrochemical properties of the high voltage spinel system are significantly dependent on their electronic properties, lattice orientations, and film thicknesses of the electrodes.

1. Introduction

Lithium ion secondary batteries have been applied not only for cellular phones and personal computers in recent years, but also for hybrid electric vehicles (HEVs) and pure electric vehicles (EVs). Such applications require a high energy density and a long working life. The energy density and cycling performance of batteries are closely related to the nature of the electrode reaction; therefore, new positive-electrode materials are required to satisfy these high performance requirements. The high-voltage $LiNi_{0.5}Mn_{1.5}O_4$ positive-electrode material with a spinel structure is one of the promising candidates for large-scale lithium ion batteries because the operating voltage is higher than those for conventional positive-electrode materials such as $LiCoO_2$ and $LiMn_2O_4$ [1–3].

Two types of structures have been reported for $LiNi_{0.5}Mn_{1.5}O_4$; one is an ordered $LiNi_{0.5}Mn_{1.5}O_4$ spinel structure with a space group of $P4_332$ and the other is a disordered spinel structure with a composition of $LiNi_{0.5}Mn_{1.5}O_{4-\delta}$ and a space group of Fd-3m. The reaction of ordered $LiNi_{0.5}Mn_{1.5}O_4$ proceeds via the Ni^{2+}/Ni^{4+} redox couple. On the other hand, the oxygen deficient disordered $LiNi_{0.5}Mn_{1.5}O_{4-\delta}$ contains trivalent manganese and exhibits two plateaus in the charge–discharge curves around at 4.1 V (Mn^{3+}/Mn^{4+}) and 4.7 V (Ni^{2+}/Ni^{4+}). The disordered $LiNi_{0.5}Mn_{1.5}O_{4-\delta}$ has the advantage of high electronic conductivity due to the Mn^{3+}/Mn^{4+} valence pair [4–8]. Although these materials provide high capacity for batteries, the main redox voltage of around 4.7 V is close to the decomposition potential

* Corresponding author. Tel./fax: +81 45 924 5401.
E-mail address: kanno@echem.titech.ac.jp (R. Kanno).

0378-7753/$ – see front matter © 2013 Elsevier B.V. All rights reserved.
http://dx.doi.org/10.1016/j.jpowsour.2013.07.051

Table 1
PLD conditions for $LiNi_{0.5}Mn_{1.5}O_4$ and $SrRuO_3$ thin films deposited on the $SrTiO_3$ (100), (110), and (111) substrates.

Target	Frequency *f*/Hz	Time *t*/min	O_2 pressure *P*/Pa	Temperature *T*/°C	Distance *d*/mm	Energy *E*/mJ
$LiNi_{0.5}Mn_{1.5}O_4$	10	15, 30, 60	6.6	650	60	150
$SrRuO_3$	5	30	10	700	60	200

for conventional electrolytes [9,10], which causes rapid capacity degradation, particularly at elevated temperatures [11,12]. The mechanism for the capacity degradation of $LiNi_{0.5}Mn_{1.5}O_4$ has previously been investigated using impedance analysis, and the interfacial resistance was found to increase with cycling [12–14]. However, a detailed interfacial reaction mechanism has yet to be clarified.

Recently, epitaxial thin films have been proposed as ideal model electrode systems to clarify surface reactions due to the following advantages [15–17]: (i) such films provide flat electrode surfaces with a roughness of 1 nm, (ii) anisotropic reaction mechanisms can be detected because the orientation of thin film can be controlled by the choice of substrate, (iii) thin film (<100 nm) nanosized electrodes can be fabricated, and (iv) the influence of the conducting material and binder can be eliminated.

In the present study, epitaxial $LiNi_{0.5}Mn_{1.5}O_4$ thin films with controlled orientations and thicknesses were synthesized on $SrTiO_3$ substrates with (100), (110) and (111) orientations. A $SrRuO_3$ layer was fabricated between the $LiNi_{0.5}Mn_{1.5}O_4$ film and the substrate as a buffer layer, which provided high electronic conductivity at the substrate and the electrode interface [18]. The effect of the $LiNi_{0.5}Mn_{1.5}O_4$ electrode orientation and thickness on the electrochemical properties was clarified.

2. Experimental

Epitaxial $LiNi_{0.5}Mn_{1.5}O_4$ thin films were grown on single-crystal $SrTiO_3$ substrates with orientations of (100), (110) or (111). A $SrRuO_3$ buffer layer was first grown on the substrate prior to deposition of the $LiNi_{0.5}Mn_{1.5}O_4$ thin films. The $SrRuO_3$ and $LiNi_{0.5}Mn_{1.5}O_4$ films were produced using a KrF excimer laser with a wavelength of 248 nm and a pulsed laser deposition (PLD) system (PLAD312, AOV Inc.). The substrates were washed with ultrapure water and annealed at 1000 °C under oxygen gas flow. After the annealing treatment, gold was deposited on both the back and lateral sides of the substrates using a sputtering system (Quick Coater SC-701, Sanyu Electron Co., Ltd.). The $LiNi_{0.5}Mn_{1.5}O_4$ target

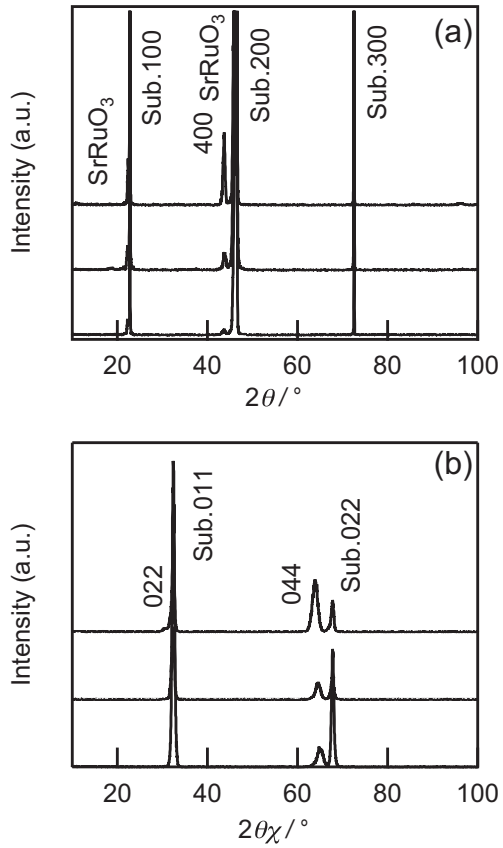

Fig. 1. XRD patterns for $LiNi_{0.5}Mn_{1.5}O_4$ thin films deposited on the $SrTiO_3$ (100) substrates: (a) out-of-plane and (b) in-plane patterns along the [011] direction of the substrates.

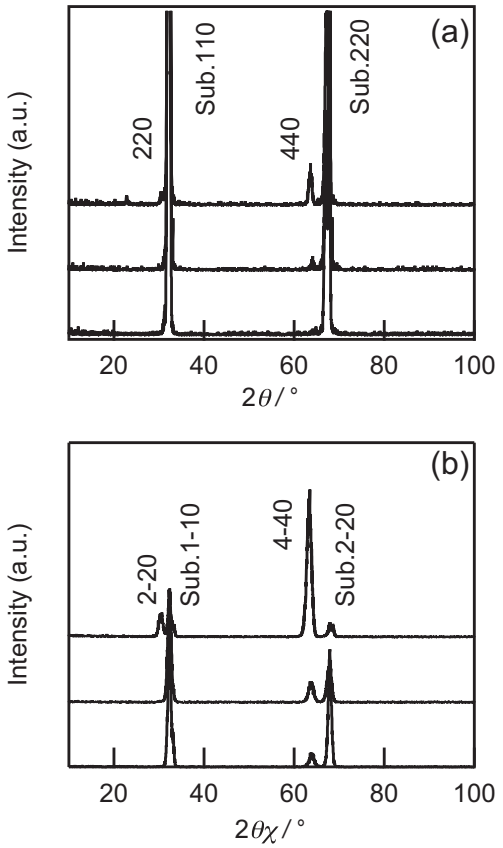

Fig. 2. XRD patterns for $LiNi_{0.5}Mn_{1.5}O_4$ thin films deposited on the $SrTiO_3$ (110) substrates: (a) out-of-plane and (b) in-plane patterns along the [1-10] direction of the substrates.

was fabricated by the solid-state reaction of Li_2CO_3, NiO, and MnO_2 starting materials that were thoroughly mixed, pelletized, and calcined at 1000 °C for 12 h, followed by subsequent heating at 700 °C for 24 h under an oxygen atmosphere. The $LiNi_{0.5}Mn_{1.5}O_4$ target had an excess lithium content [Li/(Ni + Mn) = 0.6] to compensate for lithium loss during the PLD process. Sintered $SrRuO_3$ (Toshima Manufacturing Co., Ltd.) was used as the PLD target. Table 1 summarizes the PLD conditions for each thin film. After deposition of the $SrRuO_3$ layer, the substrates were first cooled to room temperature, and then reheated to 650 °C for $LiNi_{0.5}Mn_{1.5}O_4$ deposition. The entire process for the deposition of multiple layers was performed in a vacuum chamber to avoid surface contamination.

Thin film X-ray diffraction (XRD) patterns were recorded using a diffractometer (ATX-G, Rigaku) with Cu $K\alpha_1$ radiation. The thin film orientations were characterized using both out-of-plane and in-plane measurements. The thickness, density, and surface roughness were determined by X-ray reflectivity (XRR) analysis using Parratt32 software [19].

Charge–discharge measurements were examined using 2032-type coin cells assembled in an argon-filled glove box with lithium metal as the counter electrode and the $LiNi_{0.5}Mn_{1.5}O_4$ thin film as the working electrode. The electrolyte was ethylene carbonate (EC)/diethyl carbonate (DEC) in a molar ratio of 3:7 as a solvent with a supporting electrolyte of 1 M $LiPF_6$. The charge/discharge characteristics of the epitaxial films were examined in the range of 3.2–5.0 V with a current density of 1.1 μA cm^{-2} (TOSCAT-3100, Toyo System Co., Ltd). The capacities of the thin films were calculated from the deposited area (10 × 9 mm). Ni and Mn K-edge X-ray absorption near edge structure (XANES) measurements were performed in fluorescence mode using a germanium single-element solid-state detector (Ge SSD) installed in the BL14B2 beamline at SPring-8, Japan.

Table 2
Orientation of $LiNi_{0.5}Mn_{1.5}O_4$ thin films deposited on the $SrTiO_3$ (100), (110), and (111) substrates.

Substrate orientation	$LiNi_{0.5}Mn_{1.5}O_4$ orientation	Out-of-plane	In-plane [011]	In-plane [1-10]
100	100	100	011	–
110	110	110	–	1-10
111	111	111	–	1-10

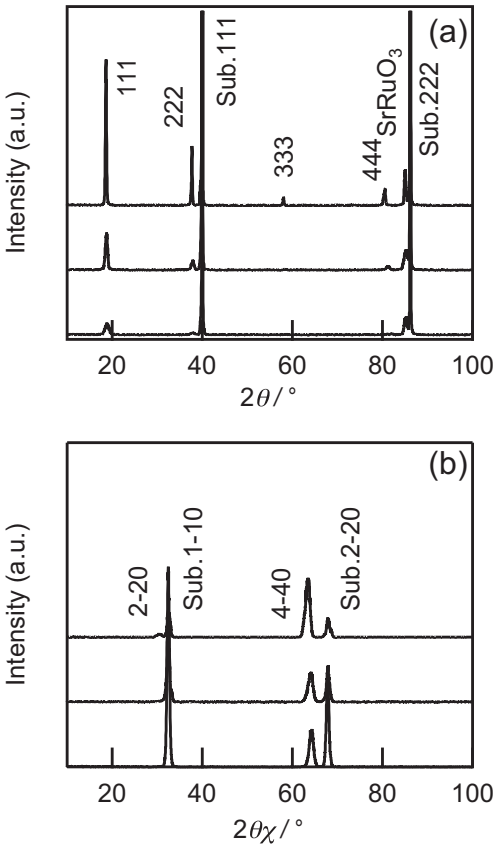

Fig. 3. XRD patterns for $LiNi_{0.5}Mn_{1.5}O_4$ thin films deposited on the $SrTiO_3$ (111) substrates: (a) out-of-plane and (b) in-plane patterns along the [1-10] direction of the substrates.

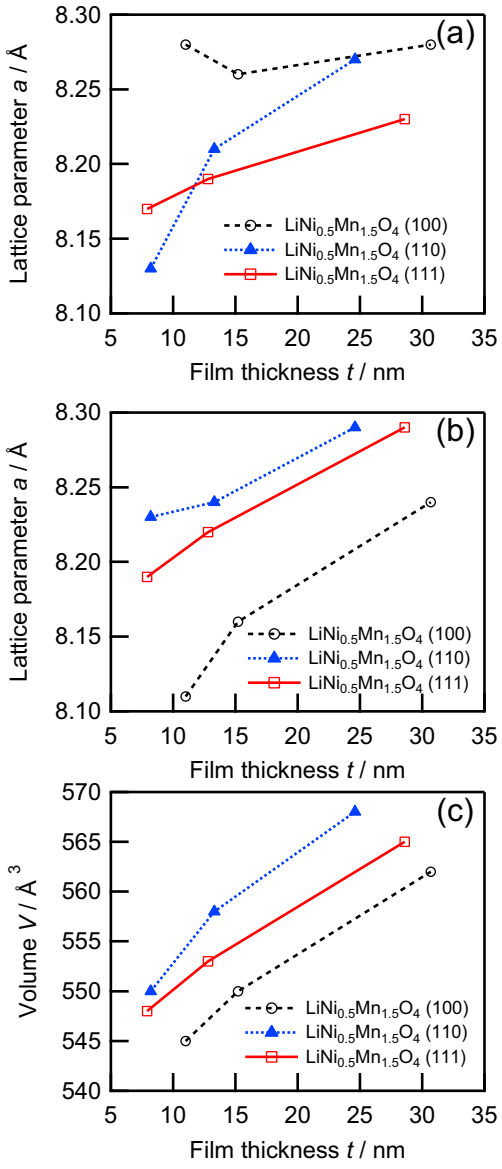

Fig. 4. Lattice parameters calculated from (a) out-of-plane and (b) in-plane measurements, and (c) the calculated unit cell volumes for $LiNi_{0.5}Mn_{1.5}O_4$ thin films deposited on the $SrTiO_3$ (100), (110), and (111) substrates.

3. Results and discussion

The crystal structure of the $LiNi_{0.5}Mn_{1.5}O_4$ thin films was characterized using XRD measurements. Fig. 1 shows both out-of-plane and in-plane XRD patterns for $LiNi_{0.5}Mn_{1.5}O_4$ thin films deposited on $SrTiO_3$ (100) substrates. The out-of-plane measurement shows a 400 reflection and the in-plane measurement along [011] shows 022 and 044 reflections. Figs. 2 and 3 show out-of-plane and in-plane XRD patterns for $LiNi_{0.5}Mn_{1.5}O_4$ thin films deposited on $SrTiO_3$ (110) and (111) substrates, respectively. The 220 and 440 reflections were observed in the out-of-plane patterns, while the 2-20 and 4-40 reflections were observed in the in-plane [1-10] patterns. The <111> direction is perpendicular to the substrate and the <1-10> direction lies parallel to the substrate. Table 2 summarizes the orientations for $LiNi_{0.5}Mn_{1.5}O_4$ thin films, where films deposited on the $SrTiO_3$ (100), (110) and (111) substrates have (100), (110) and (111) orientations, respectively. Fig. 4 summarizes the calculated lattice parameters and unit cell volumes determined from the out-of-plane and in-plane measurements. The lattice parameters and unit cell volume for the $LiNi_{0.5}Mn_{1.5}O_4$ thin films increased with film thickness. Interaction between the substrate and a deposited film typically decreases as the film thickness increases, and the lattice parameters shift toward their theoretical values. However, the lattice parameter of films with thicknesses of 24–31 nm exceeded thevalue of 8.17 Å reported for powdered $LiNi_{0.5}Mn_{1.5}O_4$ samples [3].

Fig. 5 shows an XRR spectrum, fitting curve, and scattering length density profile for $LiNi_{0.5}Mn_{1.5}O_4$ thin film deposited on an $SrTiO_3$ (111) substrate. The spectrum is plotted as a function of the scattering vector, $Qz = 4\pi\sin\theta/\lambda$, where λ is the X-ray wavelength (1.541 Å) and θ is the incident angle. A three-layer model consisting of a surface layer (impurity layer), $LiNi_{0.5}Mn_{1.5}O_4$ layer, and $SrRuO_3$ layer was applied for the data fitting. Table 3 summarizes the XRR analysis results for $LiNi_{0.5}Mn_{1.5}O_4$ and $SrRuO_3$ thin films deposited on the $SrTiO_3$ substrates. The total thickness of the $LiNi_{0.5}Mn_{1.5}O_4$ thin films was controlled from 7 to 31 nm by changing the deposition time without any significant changes occurring in the density or roughness. An impurity layer was observed on the $LiNi_{0.5}Mn_{1.5}O_4$ thin films. The surface impurity layer (d = 1.9–2.1 g cm^{-3}) is attributed to Li_2CO_3 (d = 2.1 g cm^{-3}) or LiOH (d = 1.5 g cm^{-3}). The reaction of lithium or transition metals at the surface with moisture and CO_2 in the atmosphere can lead to the formation of an impurity layer at the surface [20,21]. The density of the $SrRuO_3$ films was close to the theoretical value for $SrRuO_3$ (d = 6.3 g cm^{-3}). The density of the $LiNi_{0.5}Mn_{1.5}O_4$ layer calculated from the lattice parameter results was 4.0–4.5 g cm^{-3}.

Fig. 6 shows Ni and Mn K-edge XANES spectra for the $LiNi_{0.5}Mn_{1.5}O_4$ (111) thin films. No changes in the half-height energy ($\mu t = 0.5$) with film thickness were observed for the Ni K-edge XANES spectra, whereas those of the Mn K-edge XANES spectra shifted to lower energy with increase in the film thickness. The manganese valence decreased with increasing film thickness, which may be the result of the larger lattice parameters observed for the thicker films [22].

Fig. 7 shows initial charge–discharge curves for the $LiNi_{0.5}Mn_{1.5}O_4$ (100), (110), and (111) electrodes with various film

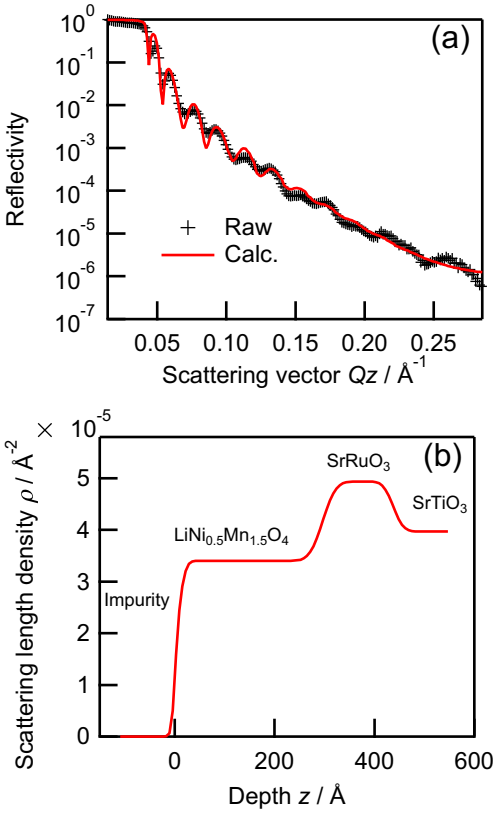

Fig. 5. (a) XRR spectrum and fitting curve, and (b) scattering length density profile for $LiNi_{0.5}Mn_{1.5}O_4$ thin film deposited on a $SrTiO_3$ (111) substrate.

Table 3
XRR analysis results for $LiNi_{0.5}Mn_{1.5}O_4$ and $SrRuO_3$ thin films deposited on the $SrTiO_3$ (100), (110), and (111) substrates.

Substrate laser time	Layer	Thickness t/nm	Density d/g cm^{-3}	Roughness r/nm
$SrTiO_3$(100)				
15 min	Impurity	1.6	1.9	0.6
	$LiNi_{0.5}Mn_{1.5}O_4$	11.0	4.2	1.1
	$SrRuO_3$	15.2	6.0	2.5
30 min	Impurity	1.4	2.0	0.8
	$LiNi_{0.5}Mn_{1.5}O_4$	15.2	4.1	1.4
	$SrRuO_3$	11.4	6.1	1.5
60 min	Impurity	1.4	2.1	0.8
	$LiNi_{0.5}Mn_{1.5}O_4$	30.7	4.0	1.0
	$SrRuO_3$	12.1	6.0	1.7
$SrTiO_3$(110)				
15 min	Impurity	5.4	2.0	1.8
	$LiNi_{0.5}Mn_{1.5}O_4$	8.2	4.4	2.1
	$SrRuO_3$	15.7	6.3	1.1
30 min	Impurity	5.9	2.0	2.1
	$LiNi_{0.5}Mn_{1.5}O_4$	13.3	4.4	1.8
	$SrRuO_3$	19.5	6.1	3.6
60 min	Impurity	5.5	2.0	1.7
	$LiNi_{0.5}Mn_{1.5}O_4$	24.6	4.1	2.3
	$SrRuO_3$	20.4	6.1	2.9
$SrTiO_3$(111)				
15 min	Impurity	1.5	2.0	0.1
	$LiNi_{0.5}Mn_{1.5}O_4$	7.9	4.4	0.7
	$SrRuO_3$	16.3	6.5	0.7
30 min	Impurity	1.6	1.9	0.1
	$LiNi_{0.5}Mn_{1.5}O_4$	12.8	4.4	0.7
	$SrRuO_3$	12.2	6.5	0.8
60 min	Impurity	1.0	2.1	0.5
	$LiNi_{0.5}Mn_{1.5}O_4$	28.6	4.3	1.0
	$SrRuO_3$	14.2	6.5	2.0

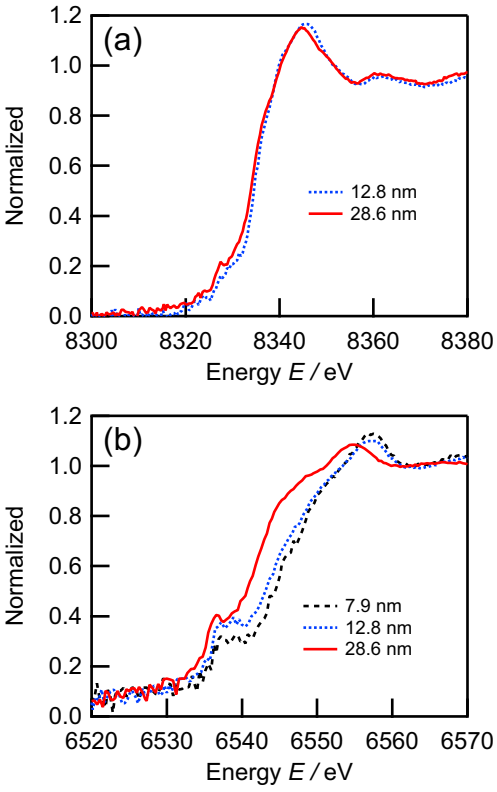

Fig. 6. (a) Ni and (b) Mn K-edge XANES spectra for $LiNi_{0.5}Mn_{1.5}O_4$ (111) thin films.

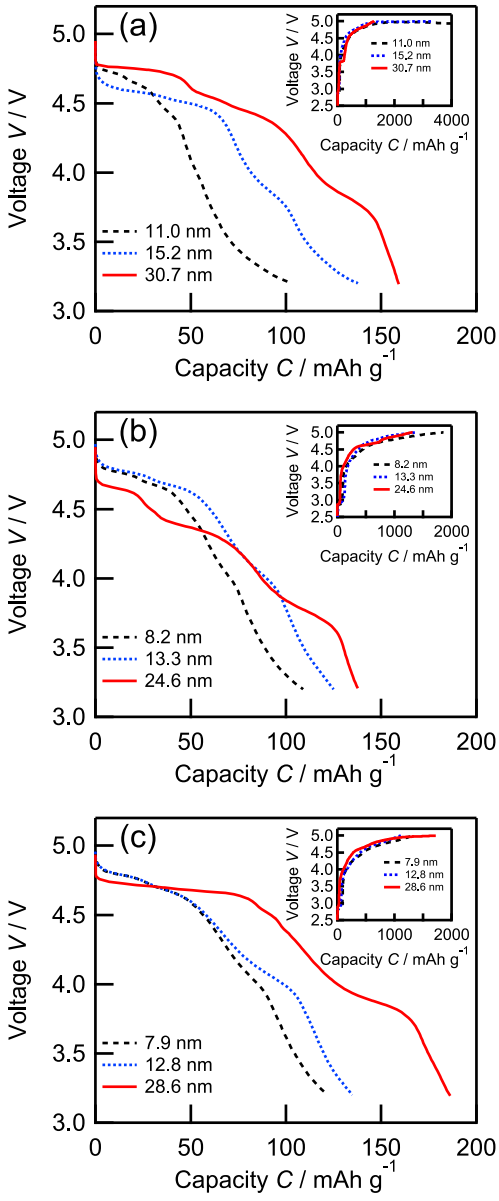

Fig. 7. Initial charge–discharge curves for (a) $LiNi_{0.5}Mn_{1.5}O_4$ (100), (b) $LiNi_{0.5}Mn_{1.5}O_4$ (110), and (c) $LiNi_{0.5}Mn_{1.5}O_4$ (111) thin films with various film thicknesses within voltage range of 3.2–5.0 V.

thicknesses. Initial charge capacities of these films exceeded the theoretical capacity. This attributed to the oxidation decomposition of electrolyte, which is especially remarkable at the high voltage electrode surface. Fig. 7(a) shows the discharge curves changed with decreasing film thickness from 30.7 to 15.2 nm for the $LiNi_{0.5}Mn_{1.5}O_4$ (100) films. For 30.7 nm-$LiNi_{0.5}Mn_{1.5}O_4$ (100), three plateaus observed around 4.7, 4.5 and 3.9 V are related to the respective Ni^{3+}/Ni^{4+}, Ni^{2+}/Ni^{3+} and Mn^{3+}/Mn^{4+} redox couples. The presence of the Mn^{3+}/Mn^{4+} redox reaction couple is characteristic of disordered spinel with an oxygen deficiency in the structure [4–8]. Discharge capacity exceeds the theoretical capacity as the lithium intercalates into the spinel structure by the following reaction below 3.2 V [23].

$$LiNi_{0.5}Mn_{1.5}O_4 + Li^+ + e^- \rightarrow Li_2Ni_{0.5}Mn_{1.5}O_4$$

Although the reaction voltage is slightly higher than those reported previously, the $LiNi_{0.5}Mn_{1.5}O_4$ surface might participate and cause a change in the reaction voltages, which cause high discharge capacity.

The Mn^{3+}/Mn^{4+} plateau in the 3.9 V region decreased and the Ni^{2+}/Ni^{4+} plateau at 4.5–4.7 V region merged into one plateau with decreasing film thickness. In additional, the increase in the capacity below 3.5 V suggests that nanosize effects are present in the epitaxial thin films [24].

The effects of thickness in $LiNi_{0.5}Mn_{1.5}O_4$ (110) and (111) films are quite similar to those observed in $LiNi_{0.5}Mn_{1.5}O_4$ (100) films as shown in Fig. 7(b) and (c). The decrease in the Mn^{3+}/Mn^{4+} plateau in the 3.9 V region with decreasing film thickness, is consistent with the higher manganese valence observed from XANES measurements.

Fig. 8 shows the cycling performance of the $LiNi_{0.5}Mn_{1.5}O_4$ (110) and (111) films with various film thicknesses. Charge capacities of all the films exceeded their theoretical capacities because of the electrolyte decomposition [9,10]. A large decrease in the capacity was observed between the 1st and 2nd discharge as shown in Fig. 8(a) and (b). On the other hand, these reactions were suppressed with decreasing film thickness (see Fig. 8(c) and (d)). Thick films which contain Mn^{3+} and oxygen deficiency cause manganese dissolution [25,26], instability of structure by Jahn–Teller effect [27,28], and then the reduced discharge capacity.

Our present study indicates that the electrochemical properties of the $LiNi_{0.5}Mn_{1.5}O_4$ surface are significantly dependent on their electronic properties, lattice orientations, and film thicknesses of the electrodes.

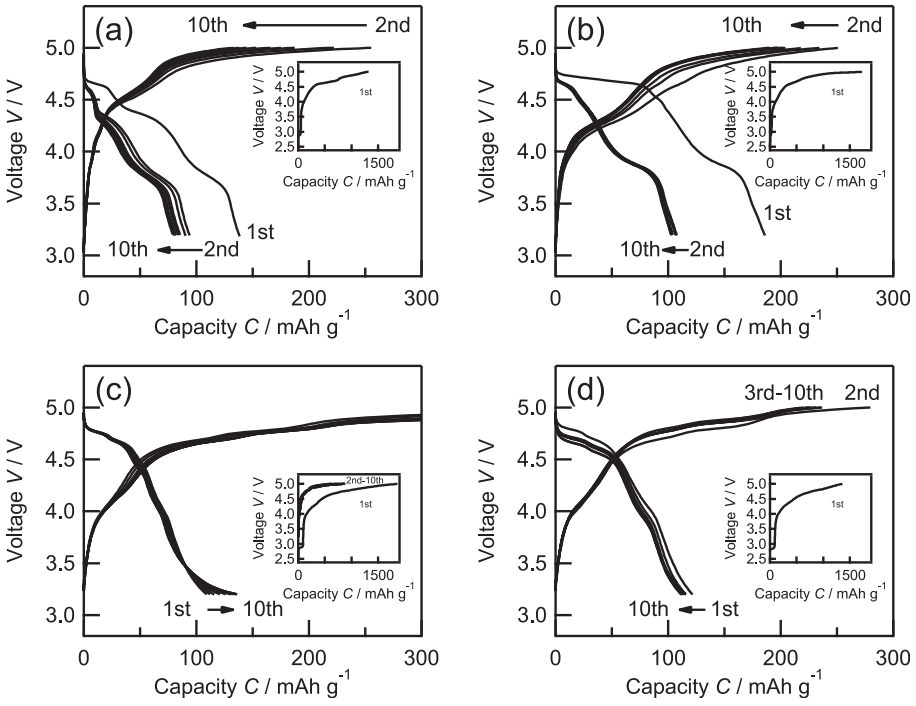

Fig. 8. Cycling performance for (a) 24.6 nm-$LiNi_{0.5}Mn_{1.5}O_4$ (110), (b) 28.6 nm-$LiNi_{0.5}Mn_{1.5}O_4$ (111), (c) 8.2 nm-$LiNi_{0.5}Mn_{1.5}O_4$ (110), and (d) 7.9 nm-$LiNi_{0.5}Mn_{1.5}O_4$ (111) thin films within voltage range of 3.2–5.0 V.

4. Conclusions

$LiNi_{0.5}Mn_{1.5}O_4$ thin films with controlled orientations and thicknesses were successfully fabricated by PLD on $SrTiO_3$ substrates with (100), (110) and (111) orientations. The lattice parameters of the films increased with film thickness, and the manganese valence decreased without any change in the nickel valence state. The discharge curves show two to three plateaus, depending on the film orientation and thickness, which correspond to the Ni^{3+}/Ni^{4+}, Ni^{2+}/Ni^{3+} and Mn^{3+}/Mn^{4+} redox couples. Oxygen vacancies may be introduced and cause the emergence of the Mn^{3+}/Mn^{4+} redox couple. Although the thick film electrodes (ca. 30 nm) exhibit a large capacity degradation between the 1st and 2nd discharge process, all the films with thicknesses in the range of 7–16 nm have rather good cycling characteristics. These epitaxial thin films exhibit good electrochemical properties and are suitable for use as model electrode systems.

Acknowledgment

The synchrotron radiation experiments were performed as projects approved by the Japan Synchrotron Radiation Research Institute (JASRI) (Proposal No. 2012B1679).

References

[1] Q. Zhong, A. Bonakdarpour, M. Zhang, Y. Gao, J.R. Dahn, J. Electrochem. Soc. 144 (1997) 205–213.
[2] T. Ohzuku, K. Ariyoshi, S. Yamamoto, Y. Makimura, Chem. Lett. (2001) 1270–1271.
[3] K. Ariyoshi, Y. Iwakoshi, N. Nakayama, T. Ohzuku, J. Electrochem. Soc. 151 (2004) A296–A303.
[4] Y. Idemoto, H. Narai, N. Koura, J. Power Sources 119–121 (2003) 125–129.
[5] J.H. Kim, S.T. Myung, C.S. Yoon, S.G. Kang, Y.K. Sun, Chem. Mater. 16 (2004) 906–914.
[6] M. Kunduraci, J.F. Al-Sharab, G.G. Amatucci, Chem. Mater. 18 (2006) 3585–3592.
[7] X. Fang, N. Ding, X.Y. Feng, Y. Lu, C.H. Chen, Electrochim. Acta 54 (2009) 7471–7475.
[8] Y.C. Jin, C.Y. Lin, J.G. Duh, Electrochim. Acta 69 (2012) 45–50.
[9] L. Yang, B. Ravdel, B.L. Lucht, Electrochem. Solid State Lett. 13 (2010) A95–A97.
[10] W. Xu, X. Chen, F. Ding, J. Xiao, D. Wang, A. Pan, J. Zheng, X.S. Li, A.B. Padmaperuma, J.G. Zhang, J. Power Sources 213 (2012) 304–316.
[11] T. Yoon, S. Park, J. Mun, J.H. Ryu, W. Choi, Y.S. Kang, J.H. Park, S.M. Oh, J. Power Sources 215 (2012) 312–316.
[12] J. Mao, K. Dai, Y. Zhai, Electrochim. Acta 63 (2012) 381–390.
[13] T. Yang, N. Zhang, Y. Lang, K. Sun, Electrochim. Acta 56 (2011) 4058–4064.
[14] Y.Y. Huang, X.L. Zeng, C. Zhou, P. Wu, D.G. Tong, J. Mater. Sci. 48 (2013) 625–635.
[15] M. Hirayama, N. Sonoyama, M. Ito, M. Minoura, D. Mori, A. Yamada, K. Tamura, J. Mizuki, R. Kanno, J. Electrochem. Soc. 154 (2007) A1065–A1072.
[16] K. Sakamoto, H. Konishi, N. Sonoyama, A. Yamada, K. Tamura, J. Mizuki, R. Kanno, J. Power Sources 174 (2007) 678–682.
[17] M. Hirayama, H. Ido, K. Kim, W. Cho, K. Tamura, J. Mizuki, R. Kanno, J. Am. Chem. Soc. 132 (2010) 15268–15276.
[18] K. Suzuki, K. Kim, S. Taminato, M. Hirayama, R. Kanno, J. Power Sources 226 (2013) 340–345.
[19] L.G. Parratt, Phys. Rev. 95 (1954) 359–369.
[20] R. Moshtev, P. Zlatilova, S. Vasilev, I. Bakalova, A. Kozawa, J. Power Sources 81–82 (1999) 434–441.
[21] K. Matsumoto, R. Kuzuo, K. Takeya, A. Yamanaka, J. Power Sources 81–82 (1999) 558–561.
[22] D. Pasero, N. Reeves, V. Pralong, A.R. West, J. Electrochem. Soc. 155 (2008) A282–A291.
[23] K. Amine, H. Tukamoto, H. Yasuda, Y. Fujita, J. Electrochem. Soc. 143 (1996) 1607–1613.
[24] M. Okubo, E. Hosono, J. Kim, M. Enomoto, N. Kojima, T. Kudo, H. Zhou, I. Honma, J. Am. Chem. Soc. 129 (2007) 7444–7452.
[25] J.C. Hunter, J. Solid State Chem. 39 (1981) 142–147.
[26] Y. Liu, X. Li, H. Guo, Z. Wang, Q. Hu, W. Peng, Y. Yang, J. Power Sources 189 (2009) 721–725.
[27] R.J. Gummow, A. deKock, M.M. Thackeray, Solid State Ionics 69 (1994) 59–67.
[28] E. Wolska, M. Tovar, B. Andrzejewski, W. Nowicki, J. Darul, P. Piszora, M. Knapp, Solid State Sci. 8 (2006) 31–36.